

THESIS FOR THE DEGREE OF LICENTIATE OF ENGINEERING

VERTICAL-CAVITY SURFACE-EMITTING
LASERS WITH IMPROVED
WIDE-TEMPERATURE PERFORMANCE

Hans Daniel Kaimre



Photonics Laboratory
Department of Microtechnology and Nanoscience - MC2
Chalmers University of Technology
Göteborg, Sweden, 2025

VERTICAL-CAVITY SURFACE-EMITTING LASERS WITH IMPROVED
WIDE-TEMPERATURE PERFORMANCE

Hans Daniel Kaimre

Göteborg, January 2025

©Hans Daniel Kaimre, 2025

Chalmers University of Technology
Microtechnology and Nanoscience - MC2
Photonics Laboratory
SE-412 96 Göteborg, Sweden
Phone: +46 (0) 31 772 1000

ISSN 1652-0769
Technical Report MC2-470

Printed in Sweden by Reproservice, Chalmers University of Technology
Göteborg, Sweden, February 2025

VERTICAL-CAVITY SURFACE-EMITTING LASERS WITH IMPROVED WIDE-TEMPERATURE PERFORMANCE

Hans Daniel Kaimre

Photonics Laboratory

Department of Microtechnology and Nanoscience - MC2

Chalmers University of Technology

Abstract

The vertical-cavity surface-emitting laser (VCSEL) is the preferred light source for high-speed and power-efficient short-reach optical interconnects (OIs) in high-performance computing systems, datacenters, and other short-range optical networks. Such OIs typically operate over a temperature range of 0 to 70 °C. However, some emerging applications of VCSEL-based OIs, such as in automotive optical networking and optical networks in some military systems, require operation over a much wider temperature range, e.g. from -40 to 125 °C. With the VCSEL being the most temperature sensitive component of the OI, and uncooled/unheated operation required for cost and power efficiency, there is a demand for VCSELs with reduced temperature dependence, operating over a wider temperature range.

The temperature dependence of VCSEL performance stems from variations in optical gain and mismatches between gain spectrum and resonance wavelength shifts. Methods to mitigate these effects include using VCSELs with appropriate gain-cavity detuning and gain engineering to broaden optical gain spectrum.

This thesis investigates 850 nm VCSELs optimized for operation over a large temperature range. Key studies include the correlation of threshold current with performance parameters (Paper A) and the design of chirped QW VCSELs to stabilize performance across temperatures (Paper B). Insights into designing robust VCSELs for extreme environments are presented.

Keywords: Vertical-cavity surface-emitting lasers, optical interconnects, wide-temperature performance, detuning, chirped QWs.

This thesis is based on the work contained in the following papers:

- [A] **Hans Daniel Kaimre**, Alexander Grabowski, Johan Gustavsson, and Anders Larsson “Effects of Detuning on Wide-Temperature Behavior of 25 Gbaud 850nm VCSELS,” Proc. SPIE 12439, Vertical-Cavity Surface-Emitting Lasers XXVII, 124390C (15 March 2023).
- [B] **Hans Daniel Kaimre**, Alexander Grabowski, Johan Gustavsson, and Anders Larsson, “25 Gbaud 850 nm VCSEL for an Extended Temperature Range,” *IEEE Photonics Technology Letters*, 2024, in review.

Other publications by the author, not included in this thesis, are:

- [C] Mohammad Bilal Aziz, **Hans Daniel Kaimre**, Peter Andrekson, “High-Speed Transmission of 850 nm VCSEL Optical Interconnects Across Wide Temperatures”, *IEEE Photonics Technology Letters*, 2024, in review.

Contents

Abstract	iii
Publications	v
Acknowledgement	ix
Acronyms	xi
1 Introduction	1
1.1 Background and motivation	1
1.2 VCSELs with reduced temperature dependence	2
1.3 In this thesis	3
1.3.1 Thesis outline	3
2 Vertical-Cavity Surface-Emitting Lasers	5
2.1 Semiconductor lasers	5
2.1.1 Laser fundamentals	5
2.1.2 Semiconductor laser principles	6
2.2 The Vertical-Cavity Surface-Emitting Laser	8
2.2.1 History	9
2.2.2 VCSEL structure	9
2.2.3 Mirrors and resonator	10
2.2.4 Active region	11
2.2.5 Electro-optical confinement	13
2.2.6 Static performance characteristics	13

2.2.7	Spectral characteristics	15
2.2.8	Dynamics	16
2.2.9	High-speed VCSELS and bandwidth limitations	18
2.3	Experimental setups	20
2.4	VCSEL fabrication	22
3	Thermal effects in VCSELS	27
3.1	Wavelength shift	27
3.2	Temperature dependence of gain	28
3.3	Wavelength detuning	29
3.3.1	Impact of wavelength detuning on VCSEL performance	30
4	Gain engineering in VCSELS	31
4.1	QW gain theory	31
4.2	Chirped QWs	33
4.3	Previous work on chirped QWs	34
4.3.1	Varying thickness	34
4.3.2	Varying composition	35
4.4	Temperature-insensitive VCSELS with chirped QWs	36
5	Future outlook	39
6	Summary of papers	41
	Included papers A–B	49

Acknowledgement

I would like to sincerely thank my supervisor, Anders, for accepting me as a PhD student and for his support throughout this journey so far. Thank you for generously giving your time and decades-long expertise, often on short notice, and for helping me navigate challenges along the way. I am especially grateful for your continued supervision even after you retired from Chalmers.

A special thanks to Alexander for showing me all the ropes in the lab and cleanroom and for teaching me most of the skills I have needed for my work. I would also like to thank Victor and Peter for their support and guidance, always being available whenever I needed their help.

To everyone in the Photonics Lab: thank you for creating a great working environment. A special mention goes out to my good friend Erik, who has been a fantastic companion both in the office and beyond.

I am also grateful to everyone in the Hot Optics project for the exciting discussions that always seemed to run out of time during our project meetings. A special thanks to Bilal, Lars, Stavros, and Siavash for helping out whenever I needed their expertise. Thank you to the staff in the nanofabrication lab who helped out with all the work in the cleanroom.

To my friends and family: thank you for your support along the way. I am grateful to my teammates at Chalmers Basket for providing a sense of purpose and fun outside of work, making life beyond the lab just as rewarding.

Finally, my deepest gratitude goes to my wife Riinu for all the support. When things got difficult at work or when I had issues with my health, you were always there for me with unconditional help and love.

Hans Daniel Kaimre
Göteborg, January 2025

Acronyms

BCB	Benzocyclobutene
CW	Continuous wave
DBR	Distributed Bragg reflector
DUT	Device under test
EEL	Edge-emitting laser
IC	Integrated circuit
ICP	Inductively coupled plasma
IPV	Current-power-voltage
IV	Current-voltage
LED	Light-emitting diode
LI	Light-current
LIV	Light-current-voltage
LP	Linearly polarized
MM	Multi-mode
MQW	Multiple quantum well
OI	Optical interconnect
PECVD	Plasma-enhanced chemical vapor deposition
PL	Photoluminescence
QD	Quantum dot
QFLS	Quasi-Fermi level separation
QW	Quantum well
RIE	Reactive-ion etching
RT	Room temperature
SCH	Separate confinement heterostructure

SG	Signal-ground
TMM	Transfer matrix method
VCSEL	Vertical-cavity surface-emitting laser
VNA	Vector network analyzer

1.1 Background and motivation

The vertical-cavity surface emitting laser (VCSEL) is a type of semiconductor laser used widely in various fields. While the first VCSEL realized by Kenichi Iga et. al [1] in 1979 operated at 77K and performed extremely poorly according to modern standards, it was a scientific breakthrough that has paved the way for the use of VCSELs in various fields in the modern world. Historically, the most important use-case of VCSELs has been as transmitters in short-reach optical interconnects. Today, the majority of GaAs VCSELs fabricated annually are used in consumer electronics, fueled mainly by Apple, whose newer iPhone models implement the devices in its Face-ID™ technology. Datacom applications, which are another major market for GaAs VCSELs, follow closely [2]. However, there is speculation that thanks to the emergence of artificial intelligence (AI) technologies, the increase of computational power of high-performance computing systems will lead to demand for higher data-rates inside these supercomputers, which means that datacom applications could regain the market dominance position in the foreseeable future.

VCSELs could be used in transceivers in additional new markets, however a number of them demand for VCSELs with sufficient performances at high temperatures and/or over a wide temperature range. To

name a few, some of these potential applications are co-packaged optics in high-performance computing units, the automotive industry and various defense/military applications.

In high-performance computing units, optical interconnects (OIs) using VCSELs have replaced electrical interconnects for short-reach data communication between different computing units. Most systems today use pluggable optical transceivers located on the front panel of the servers which convert the electrical signal into optical signal. With increasing data rates, the port density becomes excessive and the transceivers on the front panel cannot provide sufficient data rates for modern applications. Therefore to achieve a smaller footprint per transceiver, the transceivers have to migrate inside the units close to the integrated circuits (ICs), where temperature variations can be extreme and peak temperatures can exceed 100°C .

Harsh conditions, where VCSELs could prove useful, are also present in automotive applications. With the emergence of adaptive driving assistance systems and autonomous driving technologies, vehicles are using an increasing number of various sensors (cameras, radars, lidars) that all transmit a large amount of data, leading to increased intra-vehicle data rates. VCSEL-based optical interconnects could pose a solution to this challenge by meeting the demand for more energy-efficient and cheaper on-board interconnects. However, this environment is even harsher, with the automotive industry standards demanding for devices to operate sufficiently from -40 to 125°C . Similar conditions are experienced in defense and military applications. VCSELs used in these applications must therefore have a superior wide-temperature performance.

1.2 VCSELs with reduced temperature dependence

The considerable VCSEL performance dependence on ambient temperature is largely attributed to changes in optical gain and differential gain within the active region, driven by the temperature-dependent Fermi occupation probabilities. The temperature dependence is further accelerated by the different rates at which the gain spectrum and the resonance (lasing) wavelengths red-shift as the temperature increases. To mitigate these effects, earlier approaches have employed methods to spectrally broaden the optical gain. Examples include the use of quantum wells (QWs) with varying thicknesses [3–5] or quantum dots (QDs) with a size

distribution [6] in the active region, where the variation in QW and QD sizes generates optical gain across a wider range of wavelengths, thereby broadening the overall gain and leading to a decreased temperature-dependence of the device performance.

1.3 In this thesis

This thesis concentrates on the performance of 850 nm VCSELs in harsh conditions, i.e. at very cold subzero temperatures or extremely hot temperatures well above 100°C. For this purpose, several VCSEL designs optimized for performance over a wide temperature range are studied.

In Paper A, two VCSELs with otherwise similar design, but different wavelength detuning are studied. Results show that threshold current has a strong correlation with various performance parameters and minimizing variation of the threshold current over temperature is important for improving performance at very low or high temperatures.

In Paper B, two VCSEL designs intended for performance over a wide temperature range are presented. One of the presented devices uses chirped QWs in the active region, designed with the aim to minimize threshold current over temperature.

1.3.1 Thesis outline

The outline of this thesis is as follows. In Chapter 2, the basics of vertical-cavity surface emitting lasers are discussed. In Chapter 3, various thermal effects, most notably wavelength detuning, in VCSELs are discussed. Chapter 4 gives an overview of gain engineering in semiconductor lasers and VCSELs, with emphasis on chirped QW VCSELs. Finally, in Chapter 5, the future outlook is presented and Chapter 6 outlines the main results in the appended papers.

Vertical-Cavity Surface-Emitting Lasers

Lasers (name originating from the acronym LASER for light amplification by stimulated emission of radiation) are devices that produce light with both spatial and temporal coherence through optical amplification based on the stimulated emission of photons. Various types of lasers exist, with different architectures and gain mediums, including gas, chemical, solid-state, fiber, and semiconductor lasers. However, this thesis focuses solely on semiconductor lasers, with particular emphasis on vertical-cavity surface-emitting lasers (VCSELs) and effects of ambient temperature on the device performance. This chapter provides an overview of the fundamental operating principles of semiconductor lasers and examines the structure and characteristics of VCSELs in detail.

2.1 Semiconductor lasers

2.1.1 Laser fundamentals

A simplified representation of a laser's architecture is shown in Figure 2.1. The operation of a laser is founded on two key processes: optical amplification and feedback.

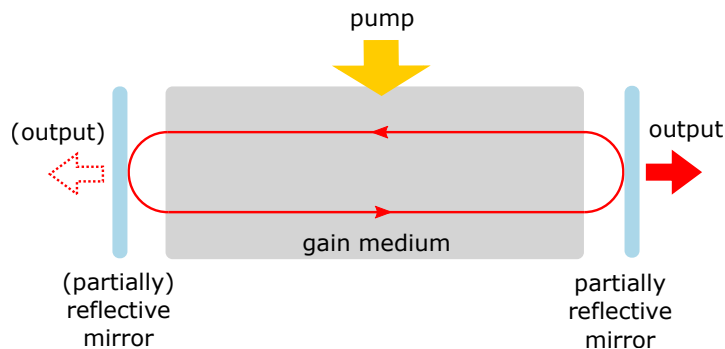


Figure 2.1: Basic design of a laser.

Optical amplification is achieved by creating a population inversion in the gain medium, which is energized by an external energy supply (e.g. electrical or optical pumping). Population inversion occurs when the majority of atoms in the gain medium are in an excited energy state. Once this condition is met, stimulated emission dominates, producing photons that share the same frequency, phase, and polarization.

To enable oscillation, the system must include optical feedback. This is typically achieved by positioning the gain medium between two parallel reflective mirrors, forming a resonator (also known as a cavity). At least one of the mirrors must be partially reflective to allow a portion of the generated light to exit the cavity as output. If both mirrors are partially reflective (as illustrated in Figure 2.1), light will be emitted from both sides of the laser.

2.1.2 Semiconductor laser principles

In a basic semiconductor laser, the electrically pumped gain medium, also known as the active region, typically consists of an undoped (intrinsic) direct band gap semiconductor material positioned between p - and n -doped materials with higher band gaps. This configuration, illustrated in the generic semiconductor laser diagram in Figure 2.2, is often referred to as an edge-emitting laser (EEL), where the cleaved end facets function as mirrors. The intrinsic region serves two key roles: it captures energetic electrons during pumping and guides the laser light. Optical guiding is facilitated by the higher band gap materials, which generally exhibit a lower refractive index.

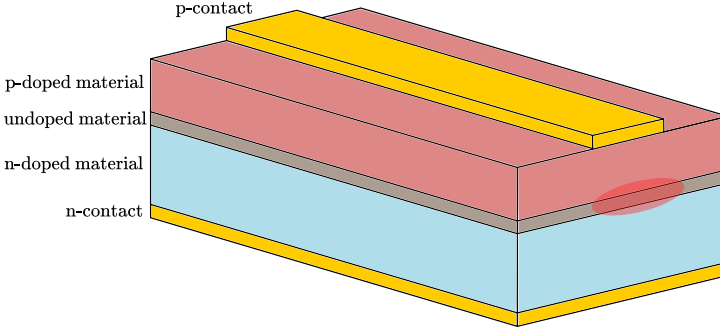


Figure 2.2: An EEL emits light perpendicularly to its epitaxial layers.

The population inversion required for lasing is achieved by injecting excess electrons and holes into the *pin*-junction through the drive current. When the *pin*-junction is forward biased, electrons and holes accumulate in the active region, leading to radiative transitions. Once the current reaches a specific value, known as the threshold current (I_{th}), the gain in the cavity equals the losses, satisfying the lasing condition. The threshold gain required can be expressed as

$$g_{th} = \frac{1}{\Gamma} \left(\alpha_i + \frac{1}{2L} \ln \frac{1}{R_1 R_2} \right), \quad (2.1)$$

where Γ is the confinement factor defined as the volumetric overlap of the optical mode with the gain medium, α_i the internal optical loss, L the length of the cavity and R_1 , R_2 the reflectivities of the two different facets of the laser. The second term in parenthesis in Equation 2.1 can be incorporated into a single parameter called the mirror loss:

$$\alpha_m = \frac{1}{2L} \ln \frac{1}{R_1 R_2}. \quad (2.2)$$

In addition to satisfying the lasing threshold condition described by Equation 2.1, the phase of the optical field must reproduce itself after a complete round trip. Mathematically, this can be expressed as

$$\exp(-j\beta \cdot 2L) = \exp\left(-j \frac{2\pi}{\lambda_0/n_{\text{eff}}} \cdot 2L\right) = 1, \quad (2.3)$$

which results in multiple solutions for the wavelength of the lasing mode, as given by

$$\lambda_0 = \frac{2Ln_{\text{eff}}}{m}, \quad (2.4)$$

where λ_0 is the wavelength of the light in vacuum, n_{eff} the effective refractive index of the mode and m an integer.

The steady-state and dynamic behaviors of a semiconductor laser can be analyzed using a set of rate equations (although this is a simplified model, it provides valuable insight into the qualitative behavior of the devices). Equation 2.5 describes the change in excess carrier density over time in the active region, accounting for various processes [7]. Equation 2.6 illustrates how this change influences the photon density of individual modes within the cavity [7]. Note that the equations describe a single-mode laser.

$$\frac{dN}{dt} = \frac{\eta_i I}{qV_a} - AN - BN^2 - CN^3 - \frac{c}{n_{g,\text{eff}}}gS, \quad (2.5)$$

$$\frac{dS}{dt} = \left[\frac{c}{n_{g,\text{eff}}}\Gamma g - \frac{1}{\tau_p} \right] S + \Gamma\beta_{\text{sp}}BN^2, \quad (2.6)$$

where N is the excess carrier density in the active region, I the injected current, η_i the internal quantum efficiency, q the elementary charge, V_a the volume of the active region, A the Shockley-Read-Hall recombination coefficient, B the spontaneous emission coefficient, C the Auger recombination coefficient, c the speed of light in vacuum, $n_{g,\text{eff}}$ the group effective index, g the gain coefficient (per unit length) and S the photon density of the mode in the cavity. Γ is the confinement factor, τ_p the average photon lifetime, given by $1/\tau_p = c/n_{g,\text{eff}}(\alpha_i + \alpha_m)$ where α_i is the internal loss coefficient and α_m the mirror loss defined by Equation 2.2, and β_{sp} the spontaneous emission factor defined as the fraction of spontaneously emitted photons that couple into the optical mode.

2.2 The Vertical-Cavity Surface-Emitting Laser

The vertical-cavity surface-emitting laser (VCSEL) is a type of semiconductor laser that differs from traditional edge-emitting lasers. Unlike EELs, where the light is emitted through the side of the chip through a cleaved facet, VCSELs emit light perpendicular to the surface of the chip, offering various advantages, e.g., miniaturization, symmetric beam properties, 2D integration, and simpler fabrication process. These improvements make VCSELs ideal for high-speed data transmission and sensing applications. Due to their compactness and efficiency, VCSELs are increasingly used in a variety of fields, with datacom networks and sensing applications being the most prominent.

2.2.1 History

The idea for the VCSEL was first proposed by Kenichi Iga in 1977 [8] and realized two years later with his colleagues in 1979 [1]. The GaInAsP/InP laser operated at a temperature of 77 K and output merely a few mW of optical output power for a driving current around 1 A. However, this achievement would be the first step in a series of scientific accomplishments laying the foundation for the multi-billion dollar market the VCSEL business is today [2]. The term "surface-emitting laser" was coined by Prof. Yasuharu Suematsu and is commonly referred to as the vertical-cavity surface-emitting laser (VCSEL) to distinguish it from other types of surface-emitting lasers, such as the second-order grating and 45-degree mirror types that emerged later [8].

These first prototypes operated in pulsed-current mode. The significant milestone of continuous-wave (CW) operation at room temperature (RT) was achieved by Iga and his colleagues in 1988 [8] and published a year later in 1989 [9]. The GaAs vertical microcavity surface-emitting laser exhibited a sub-40 mA threshold current and emitted at approximately 870 nm and achieved a maximum output power of 1.6 mW [9].

While Iga's first devices utilized bulk InGaAsP or AlGaAs active regions, the vast majority of VCSELs in production today use strained quantum wells (QWs) in the active region. The first VCSEL utilizing a strained QW active region was achieved by J. L. Jewell and his colleagues at Bell labs when they demonstrated a VCSEL with an 8 nm $\text{In}_{0.2}\text{Ga}_{0.8}\text{As}$ QW emitting at 980 nm [10]. In the same year, H. Ueno-hara, K. Iga and F. Koyama demonstrated the first VCSEL implementing multiple quantum wells (MQWs) in the active region, which helped to reduce the threshold carrier density and improve performance efficiency [11]. In the following decades, there has been numerous advances in VCSEL technology, that have been instrumental to the utilization of GaAs-VCSELs in various applications, such as short-reach OIs, sensing applications and use in every-day consumer electronics, such as Apple's iPhone's FaceID [12].

2.2.2 VCSEL structure

As the name implies, VCSELs feature a vertical resonator, in contrast to the edge-emitting lasers described in Subsection 2.1.2, where the cavity is oriented perpendicular to the layered structure. The primary benefit of this design is that it allows lasers to be processed and tested di-

rectly at the wafer level, eliminating the need for individual preparation and mounting. This significantly improves fabrication efficiency, reduces manufacturing time, and consequently lowers production costs.

Figure 2.3 illustrates a cross-section of a basic (low-speed) VCSEL design. The laser's vertical resonator is formed by two distributed Bragg reflectors (DBRs), with the top reflector being p-doped and the bottom one n-doped. Between these DBRs lies the active region, which usually contains multiple QWs.

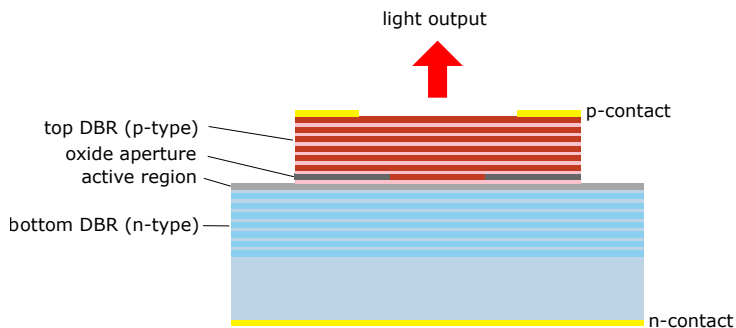


Figure 2.3: A cross-section of a VCSEL design showing two distributed Bragg reflectors (DBRs), active region, oxide aperture and contacts for current injection. Figure not to scale.

2.2.3 Mirrors and resonator

As discussed in Subsection 2.1.1, all lasers, including semiconductor lasers and thus also VCSELs, need optical feedback to enable oscillation. In VCSELs, this is typically accomplished using distributed Bragg reflectors (DBRs), which consist of quarter-wavelength thin layers made from either epitaxial (GaAs-based) or dielectric materials with alternating high and low refractive indices.

In the case of GaAs-based VCSELs, the epitaxial mirrors are almost exclusively made of $\text{Al}_x\text{Ga}_{1-x}\text{As}$ with the two different slabs having low and high Al-concentrations. For example, the devices in Paper A implement 12% and 90% Al-contents (in the low-index and high-index layers, respectively), while in Paper B the Al-content in the low-index AlGaAs layers was increased from 12% to 14% to avoid interband absorption at the higher temperatures.

The active region of a VCSEL is typically very thin, resulting in a small gain per round trip. Consequently, the mirrors must exhibit

extremely high reflectivity ($>99\%$) to ensure a high number of round trips for the light. Due to the relatively small difference in refractive indices between the low- and high-index layers, a significant number of layer pairs are required in the DBRs, usually around 20–30 pairs [13]. In Paper A, the VCSELs are designed with 22 pairs in the top p-DBR and 32 pairs in the bottom n-DBR, whereas in Paper B, these numbers are 21 and 30, respectively.

2.2.4 Active region

The VCSEL active region, placed in the cavity between the DBRs, is the region where light is amplified through stimulated emission. In modern 850-nm high speed datacom VCSEL, the active region can consist of multiple (3-5) GaAs/AlGaAs [14], InGaAs/AlGaAs [15], InAlGaAs/AlGaAs [16] or InGaAsP/InGaP [17] QWs. Among these, GaAs/AlGaAs and InGaAs/AlGaAs QWs are the most widely used today [13]. In this subsection, the emission mechanism in MQW VCSELs is discussed.

The QWs are positioned next to one another within the higher bandgap separate confinement heterostructure (SCH), separated by AlGaAs barriers. These barriers effectively trap carriers, enabling high carrier densities under adequate current injection. An illustration of a MQW active region with 3 QWs can be seen in Figure 2.4.

Electrons and holes are injected into the active region from the n-doped cladding (blue region) and p-doped cladding (red region), respectively. The energy bands facilitate carrier transport into the QWs, where they accumulate. The active region consists of multiple quantum wells separated by barrier regions. QWs are designed to confine electrons in discrete energy states due to their narrow bandgap ($E_{g,QW}$) compared to the barriers ($E_{g,barrier}$). Free electrons from the conduction band and holes from the valence band are captured into the QWs, where the energy difference between these states corresponds to the bandgap energy of the QWs, determining the energy of emitted photons. Within the QWs, electrons in the conduction band recombine with holes in the valence band when interacting with the photons, and stimulated emission occurs. The emitted photons stimulate further recombination of carriers, amplifying the optical fields. The emitted photons propagate vertically in the VCSEL, aligning with the optical cavity formed by the DBRs (not shown here). The stimulated emission generates coherent light, providing the optical output power of the VCSEL. Overall, the confinement of carriers in the QWs and the stimulated emission process result in coherent opti-

cal output power in the VCSEL. A portion of the photons generated by stimulated emission escape from the partially reflective DBR, producing the laser output.

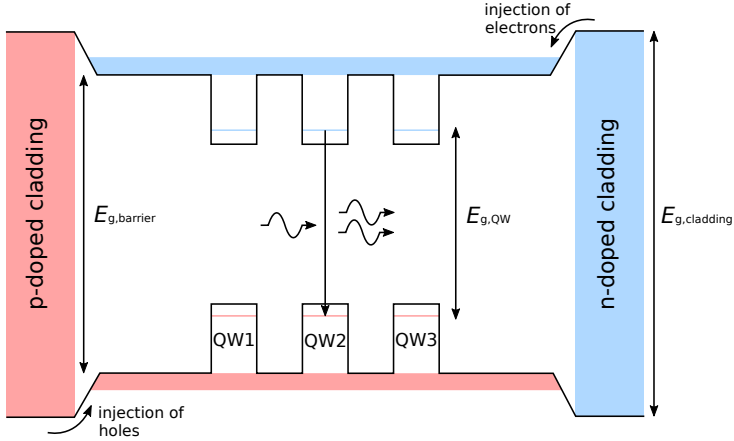


Figure 2.4: Energy band diagram of the SCH and its cladding along the vertical axis in the VCSEL, illustrating the injection of free carriers (electrons and holes) and stimulated emission. The diagram also shows the band gaps (E_g) in various regions (cladding, barriers, and QWs).

In addition to stimulated emission, VCSELs also emit light through spontaneous emission. Spontaneous emission occurs when carriers in QWs recombine spontaneously, emitting photons with random directions, polarizations, and a broader spectrum compared to stimulated emission. Additionally, non-radiative spontaneous recombination can occur. The total rate of spontaneous recombination can be expressed as [7]

$$R_{sp}(N) = A \cdot N + B \cdot N^2 + C \cdot N^3, \quad (2.7)$$

where N is the density of excess free carriers (holes and electrons), A the Shockley-Read-Hall-recombination coefficient, B the radiative recombination coefficient and C the Auger recombination coefficient. Shockley-Read-Hall and Auger recombinations are non-radiative processes, associated with defects and collisions of free carriers with excess energy, respectively [7]. Radiative recombination, as the name implies, generates photons via spontaneous emission, with only a small fraction coupled into resonator modes while the majority is lost.

2.2.5 Electro-optical confinement

The longitudinal optical confinement in VCSELs is provided by the DBRs. However, effective lateral confinement of light and current is also necessary. Historically, various methods have been employed to achieve this, including etching an air post around the top mesa [18] (with or without the regrowth of semi-insulating semiconductor) and proton implantation [19]. However, these approaches have significant drawbacks.

In the majority of VCSELs produced today, lateral confinement is achieved through selective oxidation [20], which forms an oxide aperture to confine current and light laterally. This technique is utilized in all VCSELs discussed in Paper A and Paper B. The process involves oxidizing high-aluminum AlGaAs layers using hot water vapor at elevated temperatures. In Paper B, two primary oxide layers ($\text{Al}_{0.98}\text{Ga}_{0.02}\text{As}$) and four secondary oxide layers ($\text{Al}_{0.96}\text{Ga}_{0.04}\text{As}$) are employed. In paper A, a similar design is used, however one design uses primary oxide layers with higher Al-content ($\text{Al}_{0.985}\text{Ga}_{0.015}\text{As}$), while the other design has one primary ($\text{Al}_{0.985}\text{Ga}_{0.015}\text{As}$) and one intermediate ($\text{Al}_{0.978}\text{Ga}_{0.022}\text{As}$) oxide layer. The oxidized regions serve as electrical insulators, directing current flow through the aperture, while still guiding light, since oxidized layers have a lower refractive index than the unoxidized regions in the epitaxial structure.

As a result, specific optical modes, known as oxide modes, can propagate within the cavity in the oxidized regions. Compared to the desired aperture modes, these oxide modes exhibit significantly lower gain and are blue-shifted by 15–20 nm. Nevertheless, at very low temperatures, oxide modes can dominate over the aperture modes. This phenomenon is observed in Figure 3 of Paper B, where unusual behavior in the LI curve at -40°C of one of the designs is attributed to these modes. Such behavior degrades VCSEL performance and must be accounted for in the design process of the devices through suitable selection of the thickness and vertical placement of the oxide layers.

2.2.6 Static performance characteristics

The static performance of a VCSEL is typically characterized by light-current-voltage (LIV; also know as IPV for current-power-voltage) measurements, where the device output power and applied voltage is measured vs. input electrical current.

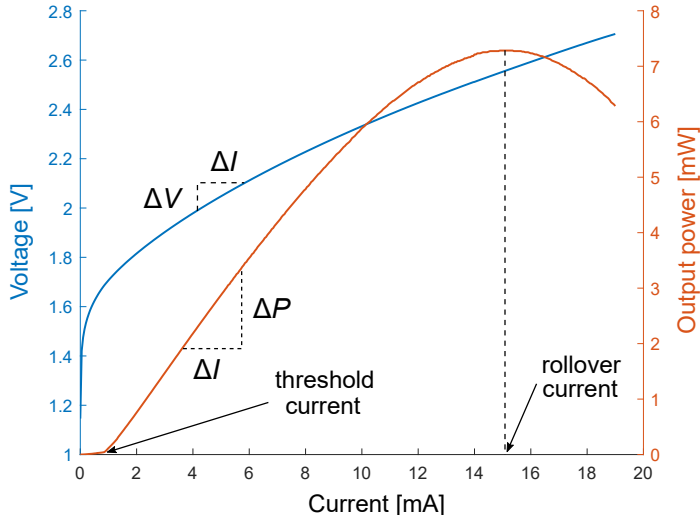


Figure 2.5: Various important static performance characteristics can be extracted from the *LIV*-curves.

A typical *LIV*-curve can be seen in Figure 2.5 with some of the important performance parameters marked:

- Threshold current I_{th} is the current required to achieve lasing in a VCSEL. Below this current, the device emits only through spontaneous emission. A lower threshold current indicates a more efficient VCSEL, as less electrical power is needed to initiate lasing. This is particularly important for minimizing power consumption in low-power applications.
- Slope efficiency $\Delta P/\Delta I$ is the rate at which optical output power increases with increasing input current above the threshold. Higher slope efficiency reflects better conversion of electrical power into optical output, making the VCSEL more energy-efficient and suitable for high-performance optical communication systems.
- Differential resistance $R_{diff} = \Delta V/\Delta I$ is the incremental resistance of the VCSEL measured from the slope of the current-voltage (*IV*) curve. It provides insight into the electrical properties of the device. Lower differential resistance indicates better current flow and reduced electrical losses, which contributes to improved efficiency and reduced self-heating.

- Roll-over current is the point at which the optical output power begins to decrease despite an increase in input current. It typically occurs due to excessive heating or carrier leakage at high currents. A higher roll-over current is desirable as it indicates a wider operational range and better thermal management in the VCSEL, leading to more stable performance at high power levels.

2.2.7 Spectral characteristics

The wavelength and power of lasing modes of a VCSEL are determined by three factors: the optical gain profile, spectral cavity response (mirror reflectivity and absorption loss) and cavity resonances (modes supported by the cavity). The width of the gain spectrum of a typical 850 nm VCSEL is on the order of few tens of nm. Because of the short cavity length, the wavelength difference between longitudinal modes (known as free spectral range, determined by equation 2.3) is on the order of few hundred nm. Therefore VCSELs only support a single longitudinal mode. However, the geometry of the device may allow for several transverse modes (lateral direction), determined mainly by the optical confinement (i.e. oxide aperture for the VCSELs presented in Paper A and Paper B).

The transverse modes that can resonate in the VCSEL are Laguerre-Gaussian modes [21], more commonly known as LP (linearly polarized) modes. Some of these lower-order modes can be seen in Figure 2.6.

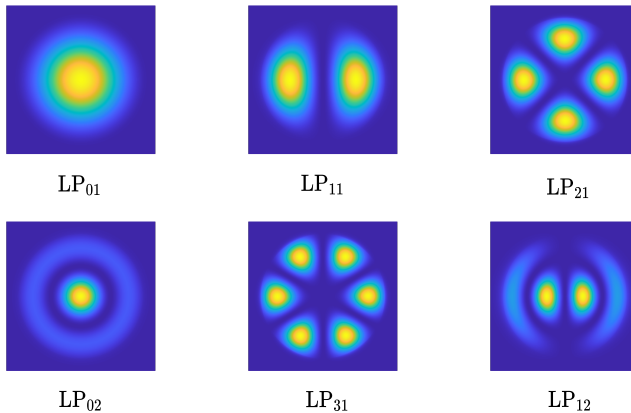


Figure 2.6: Intensity of various lower-order Laguerre-Gaussian modes.

The fundamental Gaussian (LP_{01}) mode, being the most confined, has the highest effective refractive index due to minimal interaction with the surrounding lower-index guide. Consequently, it has the longest wavelength, as the optical path length depends on the physical path multiplied by the effective refractive index. Higher-order modes resonate at shorter wavelengths. A typical spectrum for a multi-mode (MM) VCSEL can be seen in Figure 2.7, with the fundamental LP_{01} mode having the longest wavelength.

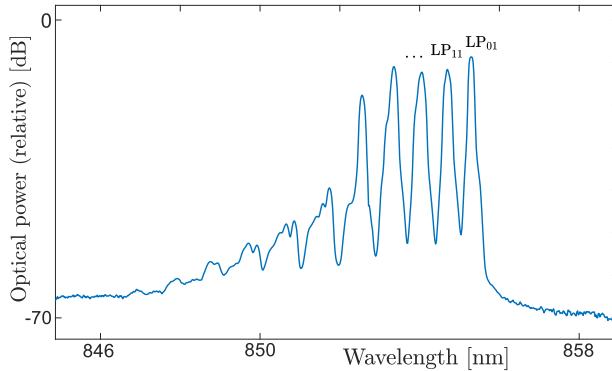


Figure 2.7: Optical spectrum of a VCSEL. Different transverse modes have different effective refractive indices and therefore different resonance wavelengths.

2.2.8 Dynamics

The basic dynamic characteristics of VCSELs can most easily be studied by analyzing the small-signal modulation response which represents the response of the output power to a small sinusoidal variation of the injection current as a function of frequency. This process is extensively described in [22].

To account for gain compression at high photon densities (i.e. currents), optical gain G can be expressed as

$$G = G(N, S) = \frac{g(N)}{1 + \epsilon S}, \quad (2.8)$$

where ϵ is gain compression factor, which accounts for gain saturation at high photon densities. Although there are no exact analytical solutions to the rate equations far away from steady state, a small perturbation

approximation can give fairly accurate results. This can be done by applying a first order Taylor expansion to I , N and S . Solving for the small-signal frequency response, the transfer function for the intrinsic response of this second order system becomes [7]

$$H_{\text{int}}(f) = \eta_d \frac{hc}{\lambda_0 q} \cdot \frac{f_r^2}{f_r^2 - f^2 + j\gamma \frac{f}{2\pi}}, \quad (2.9)$$

where η_d is the differential quantum efficiency, h the Planck constant, c the speed of light, f_r the resonance frequency (defined below) and γ the damping factor (defined below). The resonance frequency can be approximated as

$$f_r \approx \frac{1}{2\pi} \sqrt{\frac{v_g g_0 S}{\tau_p(1 + \varepsilon S)}}, \quad (2.10)$$

where g_0 is the nominal differential gain dG_0/dN (G_0 is the optical gain without gain compression; $G_0 = G(N, S = 0)$). The damping factor γ can be expressed as

$$\gamma = K f_r^2 + \gamma_0, \quad (2.11)$$

where γ_0 is the damping offset and K a parameter known as the K -factor, which can be expressed as

$$K = 4\pi^2 \left(\tau_p + \frac{\varepsilon}{v_g g_0} \right). \quad (2.12)$$

Another important parameter to characterize the dynamics of semiconductor lasers is the so-called D -factor which quantifies the rate at which the resonance frequency increases with current:

$$f_r = D \cdot \sqrt{I - I_{\text{th}}}, \quad \text{where} \quad D = \frac{1}{2\pi} \sqrt{\frac{\eta_i \Gamma v_g g_0}{q V_a}}, \quad (2.13)$$

where I is the injected current and I_{th} is the threshold current.

In addition to the aforementioned parameters, an extremely significant parameter is the 3 dB bandwidth. The modulation bandwidth is defined as the frequency at which the modulation response falls 3 dB below its low frequency value (see Figure 2.8). 3 dB bandwidth determines how fast the laser can effectively be modulated, which in turns limits the data rate of the optical link where it is used.

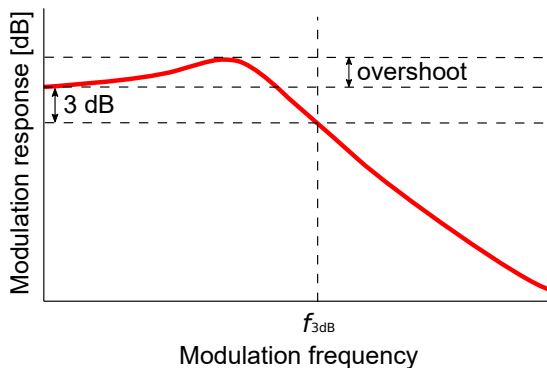


Figure 2.8: 3 dB bandwidth can be determined by studying modulation response of the VCSEL.

The resonance of the VCSEL is also described by response overshoot. Response overshoot is defined as the difference of the maximum modulation response and the modulation response at low frequencies. Excessive response overshoot can be caused by high threshold current, which reduces the difference between bias and threshold current, and thereby the resonance frequency. When the resonance frequency is reduced to below the parasitic pole frequency, the modulation response becomes more peaked. In high-speed modulation applications (such as in communication systems), large response overshoot can cause distortion in the modulated signal, resulting in pulse broadening, jitter, or signal integrity issues. These can lead to reduced data transmission rates or errors in the communication link.

2.2.9 High-speed VCSELs and bandwidth limitations

In general, VCSELs have inherently a very large modulation bandwidth. However, various techniques are used to increase the modulation bandwidth compared to a standard VCSEL design presented in Figure 2.3. This includes a careful design of the oxide layers that provide electro-optical confinement to reduce capacitance, use of strained QWs in the active region to increase differential gain, and various other techniques. The use of benzocyclobutene (BCB), an organic polymer with low dielectric constant, low optical loss, high thermal stability, and superior adhesion to various materials, reduces the parasitic pad capacitance C_p and enhances modulation speed. An illustration of a high-speed VCSEL with BCB can be seen in Figure 2.9. In addition a simplistic equivalent

circuit model is presented to explain some of the bandwidth limitations.

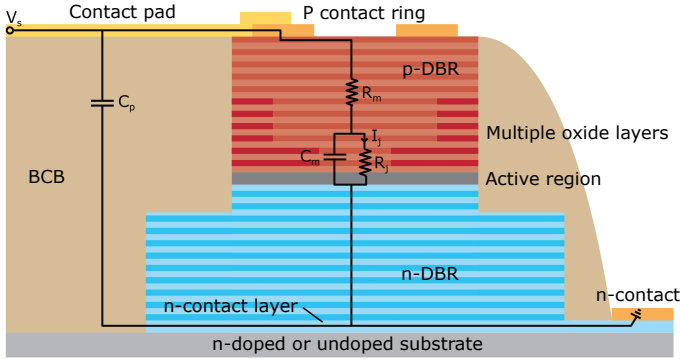


Figure 2.9: Illustration of a high-speed VCSEL with BCB with a simplified equivalent circuit model.

The bandwidth of a high-speed VCSEL is limited by several factors. Among the most significant are intrinsic modulation dynamics (damping), thermal effects, and electrical parasitics.

The intrinsic bandwidth of the VCSEL is limited by damping. At a sufficiently high bias power the damping rate becomes so large that the relaxation resonance becomes critically damped and the 3-dB bandwidth reaches a maximum value, which (without taking into account thermal and parasitic effects) can be expressed as [23]

$$f_{3\text{dB,damping}} = \frac{2\sqrt{2}\pi}{K}, \quad (2.14)$$

where K is the K -factor introduced in Subsection 2.2.8.

In addition to the intrinsic bandwidth limitation caused by damping, there are also extrinsic constraints. One extrinsic limitation is from thermal effects. As the bias current increases, the resistive components of the VCSEL and the internal optical loss generate heat due to power dissipation. This self-heating effect reduces the differential gain and increases the threshold current. Consequently, at high currents, these factors lead to a saturation of photon density and the resonance frequency.

Another extrinsic limitation arises from diffusion and depletion capacitances in the active region and the capacitance over the oxide layer(s). Together, these are referred to as the mesa capacitance. This capacitance C_m , in combination with the series resistance $R_s = R_m + R_j$, creates a low-pass RC filter (see the equivalent circuit model in Figure 2.9). This

filter shunts the the modulation current outside the active region at frequencies above the filter bandwidth.

The VCSEL transfer function, combining the transfer function representing the intrinsic response (Equation 2.9) with the transfer function representing the filtering by parasitics, becomes

$$H_{\text{tot}}(f) = \eta_d \frac{hc}{\lambda_0 q} \cdot \frac{f_r^2}{f_r^2 - f^2 + j\gamma \frac{f}{2\pi}} \cdot \frac{1}{1 + j \frac{f}{f_p}}, \quad (2.15)$$

where f_p is the cut-off frequency representing the effects of parasitics.

2.3 Experimental setups

To characterize the VCSELs, various measurements must be performed over a wide range of temperatures. In this section, different experimental setups and methods used to characterize the devices are explained.

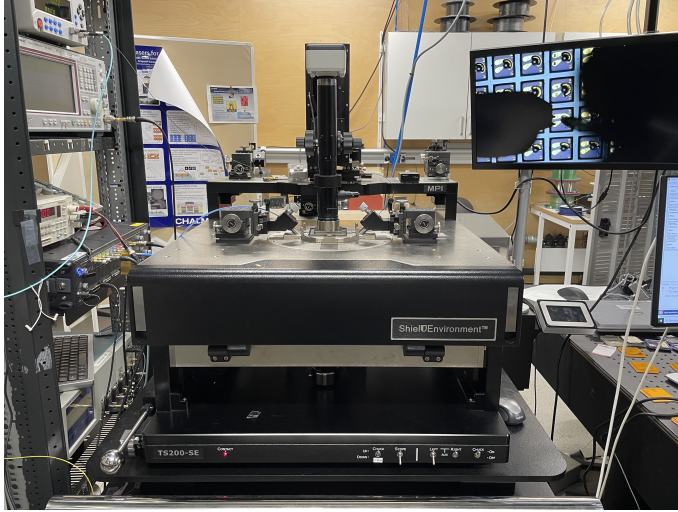


Figure 2.10: MPI TS200-SE manual probe station. A VCSEL being probed with an RF probe and output light coupled into a lensed fiber can be seen on the screen.

Since the aim of this thesis is to achieve sufficient performance of VCSELs between -40 and 125°C , the devices must also be measured in this temperature range to characterize them. To achieve this, a MPI TS200-SE manual probe station with moisture-free measurement environment, where temperature can be set from -60 to 300°C , is used. The

probe station is displayed in Figure 2.10. Devices under test (DUT) can be placed inside a temperature-controlled, moisture-free chamber. Dedicated probe arms to probe and bias the devices and couple the output light into an optical fiber, are used.

To measure *LIV*-characteristics, a large area photodetector is used. The VCSEL is biased using a Yokogawa 7651 programmable DC Source using a GGB Industries' Picoprobe customized model 40A with a signal-ground (SG) tip footprint that has a 100 μm pitch (same as the contact pitch on the VCSELs). The output light is collected using a Hamamatsu S2281 large-area Si photodiode and both the contact voltage and photocurrent of the diode (measured as voltage, corresponding to optical power) are measured by a HP 34970A data logger switch unit.

Scattering parameters (S_{11} and S_{21}) are measured using a vector network analyzer (VNA). The VCSEL is biased using a Yokogawa 7651 programmable DC supply together with a Rohde & Schwarz ZVA 67 VNA, which modulates the signal using an MPI Titan T67A probe with a signal-ground (SG) tip footprint that has a 100 μm pitch. The output light is coupled into a Thorlabs LFM1F-1 lensed tip fiber, which outputs the light into a Thorlabs DXM30BF high-speed photodetector through a EXFO FVA-3150 variable optical attenuator (used to limit the power entering the photodiode). The photodiode transforms the optical signal into an RF signal and feeds it back to the VNA. The DC source and the VNA are all controlled by a PC and the measurement results are saved by the same computer.

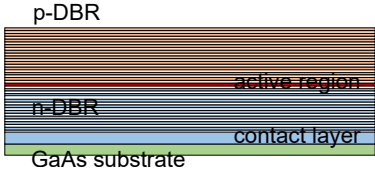
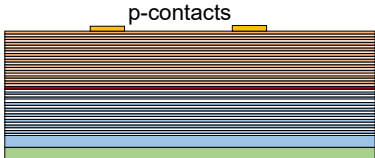
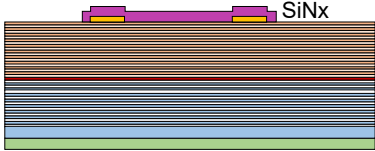
The setup to measure optical spectrum is similar to both *LIV*-setup and *S*-parameter setup. The VCSEL is biased identically as in the *LIV*-setup. The output light is coupled using a lensed fiber (as is the case for *S*-parameter measurements) directly to an ANDO AQ6317 optical spectrum analyzer.

Large-signal modulation measurements are performed as well. A 25 Gbaud NRZ signal consisting of pseudorandom binary sequences with a word length of $2^7 - 1$, generated by a bit pattern generator (SHF 12103A), is supplied to the VCSEL through a high-speed bias-T and a high-speed RF probe (MPI Titan T67A). The output light is coupled to the lensed fiber fiber, which is connected to a 32 GHz photoreceiver (MACOM PT-28F/MM) via the variable optical attenuator. The photoreceiver is connected to a 70 GHz equivalent time sampling oscilloscope (Agilent Infiniium DCA-J 86100C) to capture eye diagrams.

2.4 VCSEL fabrication

VCSELs presented in Paper B is fabricated using a mature high-speed VCSEL fabrication process developed at Chalmers over the years. A simplified overview of the process is given in Table 2.1. The attached figures represent a cross-section view of the VCSEL structure.

Table 2.1:

	Name	Figure
1	<p>Cleaving of wafers into chips. The GaAs epitaxial wafer is scribed into 8 x 10 mm chips. Each chip will have 224 individual VCSELs with varying apertures.</p>	 <p>The diagram shows a cross-section of a VCSEL wafer. From top to bottom, the layers are: p-DBR (brown), active region (red), n-DBR (blue), contact layer (light blue), and GaAs substrate (green).</p>
2	<p>Top contact deposition. Top contacts (also known as p-contacts) are deposited on the chips by evaporation. They consist of 20 nm/50 nm/100 nm Ti/Pt/Au layers.</p>	 <p>The diagram shows the same VCSEL structure as in Figure 1, but with yellow rectangular blocks representing p-contacts deposited on top of the p-DBR layer.</p>
3	<p>SiN_x deposition and photolithography to define mesa etch. Silicon nitride (also known as SiN_x) is sputtered over the entire chip to protect the unetched surfaces during the oxidation process. The circular mesa structures are defined using photolithography, and inductively coupled plasma (ICP) reactive-ion etching (RIE) is used to remove the unprotected SiN_x in an NF₃ plasma.</p>	 <p>The diagram shows the VCSEL structure with p-contacts and a layer of purple SiN_x deposited over the top. The SiN_x layer is shown as a thin purple layer covering the p-contacts and the underlying structure.</p>

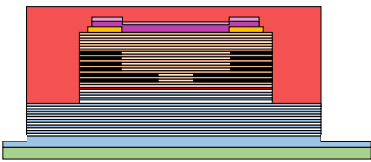
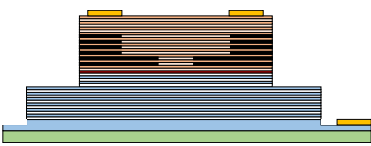
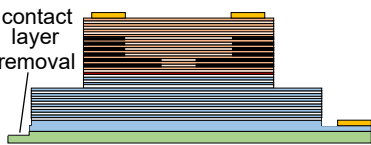
Continued on next page

Table 2.1: (Continued)

<p>4</p>	<p>Top mesa etch. The mesas are etched using Ar/SiCl₄ and Ar/Cl₂ chemistries. Four different mesa diameters (28, 30, 32, and 34 μm) are utilized to introduce variation in the final oxide aperture diameters across the chip.</p>	
<p>5</p>	<p>Protective SiN_x deposition. A protective SiN_x layer is deposited on the chip using plasma-enhanced chemical vapor deposition (PECVD) to shield the surface of the etched sample from exposure to the atmosphere and during the oxidation process.</p>	
<p>6</p>	<p>Opening of SiN_x on sidewalls. A photolithography step is performed, followed by selective NF₃ etching of the SiN_x on the mesa sidewalls to expose the 96% and 98% Al-content layers, after which the chip is oxidized.</p>	
<p>7</p>	<p>Wet oxidation. Oxide aperture is formed using wet oxidation at 420 °C.</p>	

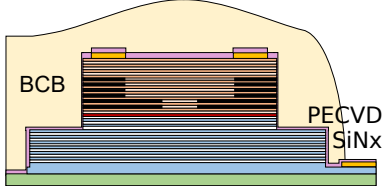
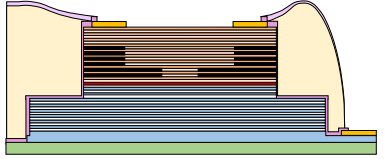
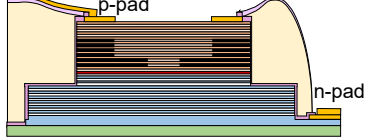
Continued on next page

Table 2.1: (Continued)

8	<p>Deep etch. Photolithography is used to define the deep etch, where secondary mesas with 50 μm diameters are etched using the same recipe as in Step 4 to etch down into the n-contact layer.</p>	
9	<p>Deposition and annealing of n-contacts. Remaining protective SiN_x is removed using the same etching procedure as in Step 3. Photolithography is used to define n-contact geometry. 20/52/100 nm thick Ni/Ge/Au n-contacts are deposited using evaporation. Germanium is incorporated into the composition because the n-contact layer lacks sufficient doping to enable ohmic contact without additional enhancement. During rapid thermal annealing for 50 s at 390 $^\circ\text{C}$ in an N_2 environment, Ge alloys with the contact layer, significantly doping it and forming ohmic contacts.</p>	
10	<p>Contact layer etch. To reduce pad capacitance, the doped contact layer beneath the area designated for the top bond pad is removed using the ICP system following a photolithography step.</p>	

Continued on next page

Table 2.1: (Continued)

11	<p>Deposition of BCB. After deposition of protective SiN_x, BCB is spun to planarize the VCSELs. The BCB is cured at 260°C in an oxygen free environment.</p>	
12	<p>Opening of mesa. Careful iterative etch (with frequent profiling to monitor the height of the remaining BCB) is performed to open up the mesa and n-contacts. Once all BCB is removed from the mesa, SiN_x is deposited on the remaining BCB for improved bondpad adhesion.</p>	
13	<p>Bondpad deposition. Ti/Au bond pads are defined using photolithography and deposited via sputtering to enable probing of the lasers.</p>	

Thermal effects in VCSELs

VCSELs are highly temperature dependent devices, with their performance significantly influenced by both external (ambient) temperature and internal heating within the device. While the mechanisms of external and internal heating differ, their effects are similar, as both lead to an increase in the temperature of the active region. Internal temperature rise in a VCSEL occurs due to power dissipation, where electrical power supplied to the laser is not entirely converted into coherent light but instead dissipated as heat. The thermal rollover mechanisms underlying this process are discussed in detail in [7, 24]. Since this thesis focuses on mitigating the impact of ambient temperature variations on VCSELs, this chapter provides an overview on how ambient temperature affects device performance.

3.1 Wavelength shift

The resonance wavelength λ of the VCSEL is a measurable parameter that depends strongly on the temperature of the device. As ambient temperature T_a or internal temperature T_i increases, a phenomenon known as the red-shift is observed in the emission spectrum, shifting it to longer wavelengths. This shift arises from temperature-induced changes in the refractive indices n of the semiconductor materials and the thermal expansion of the epitaxial layers, and it can be expressed as

$$\frac{1}{\lambda} \frac{d\lambda}{dT} = \frac{1}{\bar{n}} \frac{d\bar{n}}{dT} + \frac{1}{L} \frac{dL}{dT}, \quad (3.1)$$

where $d\bar{n}/dT > 0$ and $dL/dT > 0$. The shift induced by the change of the refractive index (first term on the right in Equation 3.1) dominates, as it is more than an order of magnitude larger than the shift induced by the increase of the cavity length (second term on the right in Equation 3.1) [25]. An example of the wavelength shift without internal heating taken into account can be seen in Figure 3.1, where the wavelength shift for one of the designs described in Paper A is displayed.

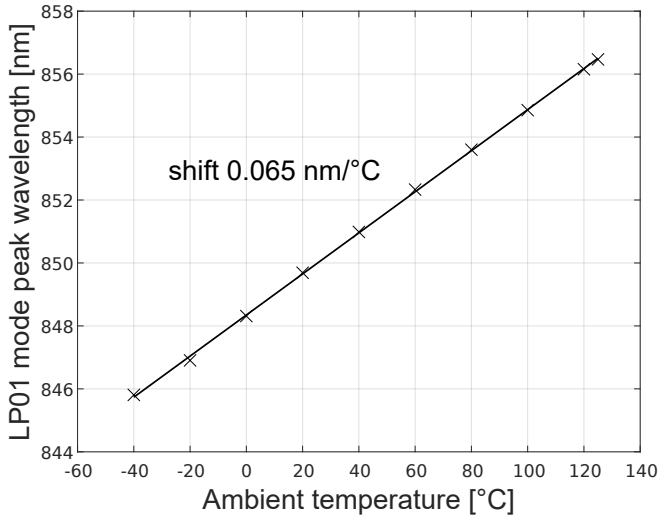


Figure 3.1: The wavelength shift of a VCSEL without any internal heating.

3.2 Temperature dependence of gain

When the temperature of an InGaAs/AlGaAs MQW VCSEL increases, the optical gain spectrum in general experiences a red-shift and a reduction of its amplitude, which can be attributed to several interrelated factors.

The red-shift is mainly caused by the decrease of the bandgap of the InGaAs QWs. This can be described by the Varshni equation [26]

$$E_g(T) = E_g(0) - \frac{\alpha T^2}{T + \beta}, \quad (3.2)$$

where $E_g(T)$ is the temperature-dependent bandgap, and α and β are material-specific constants. As the bandgap decreases, the peak wavelength of the material's optical gain spectrum shifts to longer wavelengths, for InGaAs/AlGaAs QWs this shift rate is typically around $0.33 \text{ nm}/^\circ\text{C}$.

Another important mechanism behind the reduction of the gain as temperature increases is the broadening of the Fermi occupation probability distribution, which spreads the carriers over a larger energy range for a given overall carrier density [7]. This leads to a reduced spectral concentration of inverted carriers, causing the gain spectrum to broaden and flatten [7].

At higher temperatures, non-radiative recombination mechanisms, such as Auger recombination and defect-related recombination, become more significant [7]. This reduces the number of carriers available for radiative recombination, further decreasing the gain.

Lastly, at elevated temperatures, optical loss due to free-carrier absorption in the doped DBRs increases. Additionally, intervalence band absorption can become more pronounced, leading to further optical losses that diminish the net gain.

3.3 Wavelength detuning

As discussed in Sections 3.1 and 3.2, the gain peak shifts at a rate of $0.33 \text{ nm}/^\circ\text{C}$, while the resonance wavelength, determined by the cavity length, shifts at approximately $0.07 \text{ nm}/^\circ\text{C}$. This will have a considerable effect on the performance of the VCSELs over a wide temperature range. This effect is quantified by wavelength detuning (also known as gain-cavity offset), here defined as the wavelength difference between cavity resonance and active region photoluminescence (PL) peak at room temperature (RT), illustrated in Figure 3.2. There is an approximately 10 nm to 20 nm offset between the photoluminescence (PL) and gain peak wavelengths, with the gain peak occurring at a longer wavelength. However, both peaks shift at the same rate with temperature.

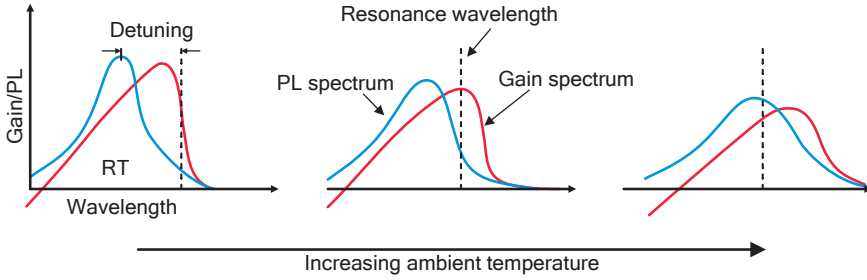


Figure 3.2: Schematic illustrating how PL and gain spectra and resonance wavelength shift with temperature. Gain and PL spectra are not to scale.

3.3.1 Impact of wavelength detuning on VCSEL performance

Detuning has strong impact most explicitly on the temperature dependence of threshold current. This is because modal gain is highly dependent on the spectral overlap between the cavity mode and the gain spectrum. A detuned system may already operate near the edge of the gain spectrum. As temperature increases, the gain spectrum shifts further, potentially reducing the effective gain below the threshold requirement. The VCSEL then requires a higher injected current to compensate, further increasing the threshold current.

Moreover, differential gain is reduced with increasing carrier density and therefore depends on threshold current which sets the carrier density due to clamping. It is also important to note that differential gain drops less rapidly on the short wavelength side of the gain peak than on the long wavelength side, which has a substantial impact on the modulation dynamics of the VCSEL and its temperature dependence.

The effect of detuning on various performance parameters from -40 to 125 °C is in detail discussed in Paper A, where two VCSELs with otherwise similar design, but different detuning are thoroughly characterized and compared.

Gain engineering in VCSELs

The phenomena that cause the strong temperature-dependence of VCSEL performance, mainly the red-shift of cavity resonance and gain and the reduction of gain with increase of temperature, discussed in the previous chapter, are mostly inherent and there is not much one can do about it. Therefore, already in 1992 it was proposed that using different QWs in a MQW active region would stagger the gain spectrums of the individual QWs, broaden the optical gain and therefore reduce the effects of temperature on the threshold current of VCSELs [27]. There are several methods to do this, for example varying the QW thickness [3–5] or QW composition (our work in Paper B). In addition, implementing QDs with a size distribution [6] in the active region, where different size QDs produce optical gain at different wavelengths, is possible. In this chapter, previous and our work on gain engineering is discussed.

4.1 QW gain theory

The gain spectrum of a MQW VCSEL under a specific bias (i.e. for a given carrier concentration) is primarily determined by the composition and architecture of the active region, which typically consists of three to five individual QWs. When designing the MQW active region with a certain number of QWs, four key parameters can be adjusted: the thickness and composition of the QWs, as well as those of the barriers

separating them. This section discusses the impact of QW composition and thickness on the gain characteristics.

Several studies have explored the influence of QW thickness and composition on the gain spectrum and overall device performance. To enable high-temperature operation and ultra-low thresholds for VCSELs emitting at 891 nm at RT used in Cs-based chip-scale atomic clocks, Zhang et al. designed three InGaAs/AlGaAs active regions with gain peak wavelengths of 870 nm, 880 nm, and 890 nm, corresponding to gain-cavity detunings of -21 nm, -11 nm, and -1 nm, respectively [28]. Based on theories developed in [29,30], they demonstrated that for a fixed indium content, increasing the QW thickness red-shifts the gain peak due to reduced quantization energies [31]. Similarly, increasing the indium content for a fixed QW thickness also red-shifts the gain peak, primarily due to a reduction of the bandgap of the InGaAs bulk material [28].

In Figure 4.1, this behavior is illustrated by plotting the peak gain wavelength vs different QW thicknesses. The calculations are performed using SimuLase [32], that uses an $8 \times 8 - \mathbf{k} \cdot \mathbf{p}$ -model to calculate the single particle wavefunctions and energies (subbands), with the model used described in more detail in [33]. The wavefunctions and subbands are used to set up the matrix elements that enter the semiconductor-Bloch equations [34, 35] that are used to calculate the gain/absorption and carrier induced refractive index changes. The structure simulated is a single $\text{In}_x\text{Ga}_{1-x}\text{As}$ quantum well, surrounded by two 10-nm-thick $\text{Al}_{0.37}\text{Ga}_{0.63}\text{As}$ barriers, on top of GaAs cladding, similar to the design used for the VCSELs in Paper B.

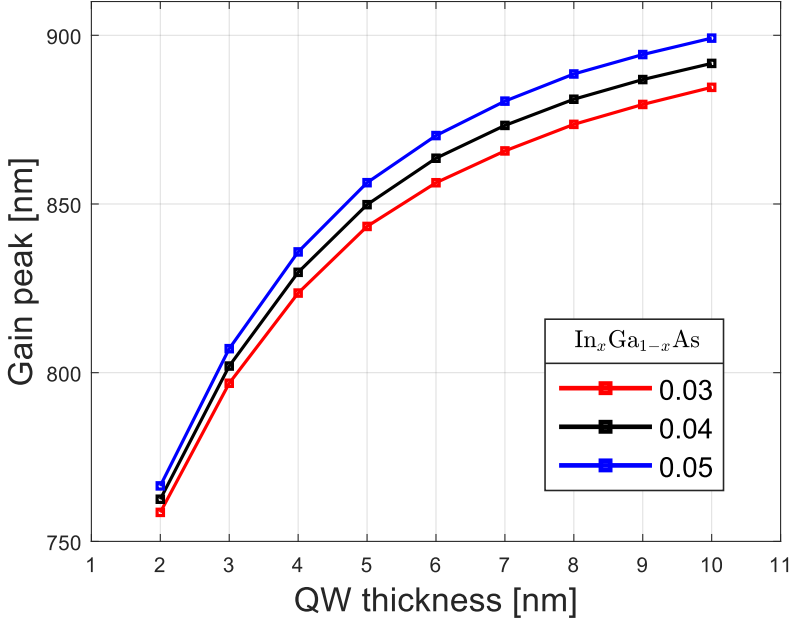


Figure 4.1: Dependence of gain peak wavelength at room temperature on QW thickness and In-content for an $\text{In}_x\text{Ga}_{1-x}\text{As}/\text{Al}_{0.37}\text{Ga}_{0.63}\text{As}$ QW. The carrier density in the QW is approximately $6 \times 10^{18} \text{ cm}^{-3}$.

It is apparent that choosing an appropriate QW thickness and composition can be used to spectrally position the gain of a MQW VCSEL. Combining QWs with different compositions or thicknesses (also known as chirped QWs) can thus be used to broaden the gain spectrum.

4.2 Chirped QWs

Chirped QWs in InGaAs/AlGaAs VCSELs are designed to improve device performance over temperature by broadening the gain spectrum and enhancing carrier confinement. In a chirped QW structure, the thickness or composition of the QWs is varied across the active region, allowing for a range of emission wavelengths. This means that the gain spectra for individual QWs will be shifted relative to each other and total gain spectrum flattened. This approach reduces the effects of gain saturation and spectral hole burning, enabling higher output power, reduced threshold currents, and improved temperature stability.

This effect is illustrated in Figure 4.2, where the simulations of modal gain at threshold of VCSELs presented in Paper B are shown. Individual QWs with different composition and equal thickness provide peak gain at different wavelengths and the total modal gain for the VCSEL with chirped QW is broadened and flattened compared to a similar VCSEL design with equal QWs. A broader gain spectrum results in more temperature-insensitive performance. These simulations are performed in SimuLase according to the same scheme as described in Section 4.1.

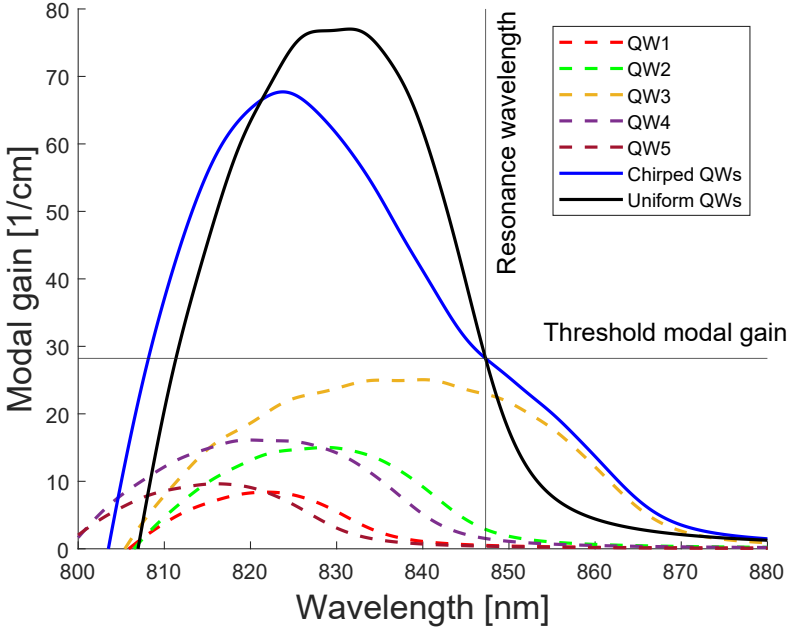


Figure 4.2: Modal gain spectrum of individual QWs (dashed); total modal gain spectrum of a VCSEL with chirped QWs (blue); modal gain spectrum of a similar MQW VCSEL with equal QWs (black).

4.3 Previous work on chirped QWs

4.3.1 Varying thickness

In 1992, Corzine et al. proposed the use of QWs with different widths in a MQW active region to broaden the optical gain spectrum [27]. In 1999, Ortiz et al. were the first to implement chirped QWs with varying thickness to demonstrate temperature-insensitive cryogenic VCSELs

providing a high-modal gain over a broad range of temperatures (5 to 350 K) and maintaining mode-gain alignment from 5 to 100 K, operating at 800 nm wavelength [3]. Their active region consisted of four GaAs MQWs of different thickness (55, 70, 90, and 105 Å), with the wells separated by 100 Å thick $\text{Al}_{0.15}\text{Ga}_{0.85}\text{As}$ barriers. In their comparison with a similar design with uniform QWs, they demonstrated the improved performance of the chirped MQW structure at both the lower and higher temperature regimes [3].

In addition there has been work implementing chirped QWs in devices other than VCSELs. Oh et al. used chirped QWs with varying thicknesses in AlGaInP-based light-emitting diodes (LEDs) and were able to demonstrate broadening of emission spectrum by 65% and increase of the light output power by 8% in comparison to LEDs with conventional MQWs [4]. Gingrich et al. have demonstrated widely tunable low-threshold current laser diodes, where the use of QWs with varying thicknesses helped improve tunability of the devices considerably [5].

4.3.2 Varying composition

As shown in Section 4.1, the optical gain spectrum is determined by both the composition and thickness of the individual QWs in a MQW active region. Thus chirped QWs can also be achieved by varying the composition of the QWs, as opposed to thickness, work on which was discussed in the previous section.

In 1995, Fritz et al. presented broad-band LEDs emitting from 1.4 μm to 2.0 μm using variable-composition InGaAs QWs [36]. Utilizing three $\text{In}_x\text{Ga}_{1-x}\text{As}$ QWs (with $x = 0.4, 0.53, \text{ and } 0.66$) embedded in the p-doped region of an InAlAs p-n junction diode, they demonstrated broad-band emission over a large wavelength range [36].

In the same year, Kajita et al. demonstrated temperature-insensitive 980 nm InGaAs/AlGaAs VCSELs using three QWs in the active region with different compositions, with gain peaks set to 970 nm, 980 nm, 990 nm, respectively [37]. The results of gain-spectrum measurements confirmed that the gain bandwidth was broader compared to conventional devices with active layers made of a single type of QWs and temperature characteristic measurements revealed that the operational temperature range of a VCSEL with a broad gain bandwidth was over 20 °C wider than that of conventional devices [37].

4.4 Temperature-insensitive VCSELs with chirped QWs

As discussed, chirped QWs can be used to broaden the optical gain spectrum and thus reduce the temperature dependence of threshold current and various other performance parameters, making the devices more temperature-insensitive. However, the individual QWs used in the MQW active region must be chosen appropriately to achieve most optimal performance. For this, extensive simulations can and should be performed. To develop the designs presented in Paper B, the following simulation process was utilized.

First, the quasi-Fermi level separation (QFLS) and gain spectrum are calculated for 4 nm thick $\text{In}_x\text{Ga}_{1-x}\text{As}/\text{Al}_{0.37}\text{Ga}_{0.63}\text{As}$ individual QWs with different compositions at different carrier densities n and temperatures T using SimuLase [32] according to the same scheme as described in Section 4.1. Then, 1D transfer matrix method (TMM) resonator simulations are used to calculate the optical confinement factor Γ for each of the QWs, resonance wavelength λ , and the modal gain at threshold (g_{th}) at the same temperatures as the SimuLase simulations are performed. Temperature dependent optical loss, caused by temperature dependent free carrier absorption in the DBRs, is accounted for.

Next, for a set of QWs with given compositions, and under the assumption of mutual thermal equilibrium (i.e. a single set of quasi-Fermi levels to represent the population of states in all QWs), the QFLS is increased until the modal gain reaches threshold. This is done over temperature and at each temperature the carrier density in the QWs at threshold is monitored. The illustration of this iterative algorithm can be seen in Figure 4.3,

At threshold, carrier injection balances spontaneous carrier recombination in the QWs. Under the assumption that carrier recombination is dominated by spontaneous emission, threshold current becomes proportional to threshold carrier density squared:

$$I_{\text{th}} = \frac{qV_a}{\eta_i} \cdot R_{\text{sp}}(\Delta n_{\text{th}}), \quad (4.1)$$

$$R_{\text{sp}}(\Delta n_{\text{th}}) = A \cdot \Delta n_{\text{th}} + B \cdot \Delta n_{\text{th}}^2 + C \cdot \Delta n_{\text{th}}^3 \approx B \cdot \Delta n_{\text{th}}^2, \quad (4.2)$$

$$\Rightarrow I_{\text{th}}(T) \sim \eta_i^{-1}(T) \cdot B(T) \cdot \Delta n_{\text{th}}^2(T). \quad (4.3)$$

While also the internal quantum efficiency η_i and B -coefficient are dependent on temperature, the sum of carrier densities squared in the

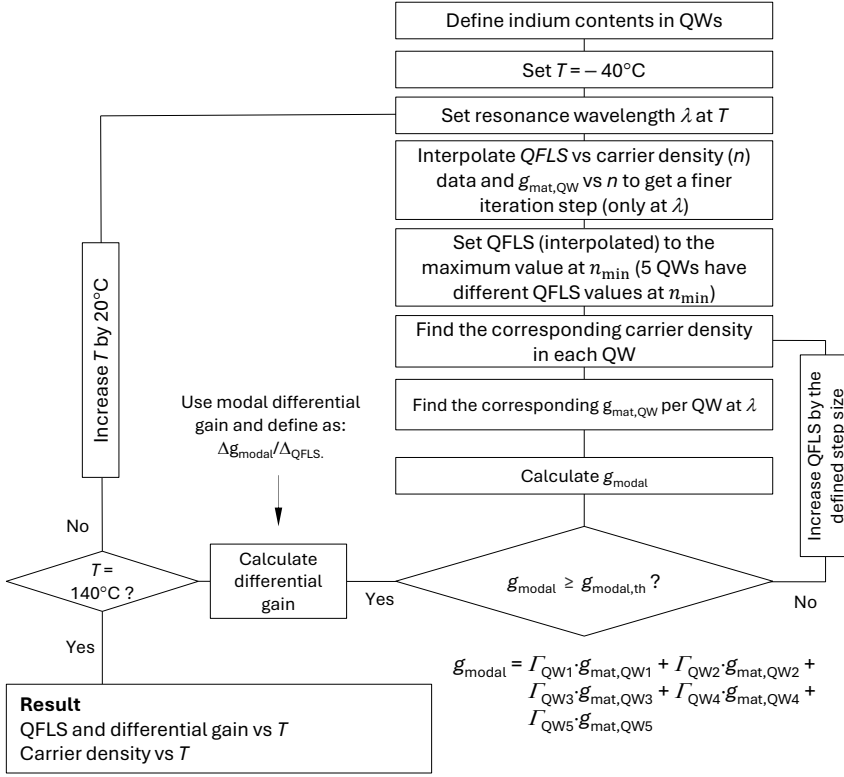


Figure 4.3: Simulation algorithm to estimate temperature dependence of threshold current.

five QWs ($\Sigma_{\text{QW}} \Delta n_{th}^2(T)$) can be used as a measure of the threshold current. In paper B, this method was used to simulate more than 100 000 different combinations.

In the paper, the design and performance of a 25 Gbaud class 850 nm VCSEL with reduced temperature dependence through the use of chirped QWs is presented. Reduced temperature dependence of threshold current, modulation bandwidth, and damping of the modulation response from -40 to 125°C is demonstrated. This work, to my knowledge, is the first to report such data rates for an 850 nm datacom VCSEL with chirped QWs in the active region over an extended temperature range from -40 to 125°C .

Future outlook

There are several research topics related to this thesis that can be explored in future upcoming work. In this chapter, some of these potential research opportunities to build upon the work presented in Paper A and B are presented.

Paper A explores the impact of detuning on the wide-temperature performance of VCSELs. While the underlying physical phenomena responsible for temperature dependencies are addressed briefly, a more in-depth analysis could provide a comprehensive understanding of the factors contributing to performance degradation at extreme temperatures. Such insights would be invaluable for designing more robust and efficient VCSELs.

In Paper B, we design, fabricate, and evaluate the performance of temperature-insensitive 850 nm datacom VCSELs. Key performance parameters are presented, along with results from large-signal transmission experiments. In Paper C, which is outside the scope of this thesis, bit-error-rate measurements were conducted using these VCSELs. Future work could explore utilizing these VCSELs as transmitters in OIs with higher-order modulation formats, advanced forward error correction, and various equalization techniques to achieve even higher data rates at temperature extremes.

Additionally, the techniques demonstrated in Paper B can be adapted to design and fabricate temperature-insensitive datacom VCSELs operat-

ing at 980 nm. Shifting to a longer wavelength offers several advantages, including enhanced differential gain, improved thermal conductivity of the Bragg mirror, reduced turn-on voltage, minimized thermal escape of carriers from QWs, lower variability in wearout, and greater robustness compared to 850 nm VCSELs [38]. These are some of the reasons why 980 nm has been chosen as the industry standard for automotive optical interconnects [39].

Paper A

Effects of Detuning on Wide-Temperature Behavior of 25 Gbaud 850nm VCSELs

SPIE Photonics West, Vertical-Cavity Surface-Emitting Lasers XXVII, published March 2023

Wavelength detuning is a prime parameter for controlling the temperature dependence of VCSEL performance. In Paper A, we study the impact of detuning on the performance of 25 Gbaud class 850 nm VCSELs over a temperature range of -40 to 125°C , as applicable to e.g. automotive optical networking. Two VCSELs with different detuning, but otherwise identical are compared. Basic static and dynamic performance parameters and their temperature dependencies are extracted. The results show that detuning can be used to engineer the VCSEL design for sufficient performance at the temperature extremes and improved tolerance to temperature variations.

My contribution: I conducted all the measurements and data analyses. I am the primary author of the paper and I presented the results at the conference.

Paper B

25 Gbaud 850 nm VCSEL for an Extended Temperature Range

IEEE Photonics Technology Letters, submitted November 2024

In Paper B, we investigate the performance of a 25 Gbaud 850 nm vertical-cavity surface-emitting laser (VCSEL) with reduced temperature dependence from -40 to 125 °C. The VCSEL design implements chirped quantum wells (QWs) with different compositions to broaden the gain spectrum and achieve sufficient performance over the entire temperature range at constant bias current and modulation voltage. A $6\text{ }\mu\text{m}$ oxide aperture diameter VCSEL supports data transmission at 25 Gb/s NRZ from -40 to 125 °C with 8 mA bias current and 640 mV modulation voltage. The temperature dependencies of basic performance parameters are also compared to those of a conventional VCSEL with identical QWs.

My contribution: I performed large parts of the simulations in the design process of the VCSEL. I fabricated the VCSELs and conducted all the measurements and data analyses. I am the primary author of the paper.

References

- [1] H. Soda, K. Iga, C. Kitahara, and Y. Suematsu, “GaInAsP/InP surface emitting injection lasers,” *Japanese Journal of Applied Physics*, vol. 18, no. 12, p. 2329, Dec 1979.
- [2] A. Jaffal, P. Boulay, M. Vallo, and E. Dogmus, “VCSELs market outlook in consumer sensing and data communication,” in *Vertical-Cavity Surface-Emitting Lasers XXVIII*, C. Lei and K. D. Choquette, Eds., vol. 12904, International Society for Optics and Photonics. SPIE, 2024, p. 1290409.
- [3] G. Ortiz, C. Hains, B. Lu, S. Sun, J. Cheng, and J. Zolper, “Cryogenic VCSELs with chirped multiple quantum wells for a very wide temperature range of CW operation,” *IEEE Photonics Technology Letters*, vol. 8, no. 11, pp. 1423–1425, 1996.
- [4] H. S. Oh, J.-M. Park, S. H. Jeong, J.-B. Park, T. Jeong, H. J. Lee, J. S. So, and K. N. Jeon, “Realization of broad-spectrum using chirped multi-quantum well structures in AlGaInP-based light-emitting diodes,” *Journal of Nanoscience and Nanotechnology*, vol. 21, no. 7, p. 3824–3828, Jul. 2021.
- [5] H. Gingrich, D. Chumney, S.-Z. Sun, S. Hersee, L. Lester, and S. Brueck, “Broadly tunable external cavity laser diodes with staggered thickness multiple quantum wells,” *IEEE Photonics Technology Letters*, vol. 9, no. 2, pp. 155–157, 1997.

- [6] N. Ledentsov, M. Agustin, V. Shchukin, J.-R. Kropp, N. Ledentsov, L. Chorchos, J. Turkiewicz, Z. Khan, C.-L. Cheng, J. Shi, and N. Cherkashin, "Quantum dot 850 nm VCSELs with extreme high temperature stability operating at bit rates up to 25 Gbit/s at 150 °C," *Solid-State Electronics*, vol. 155, pp. 150–158, 2019.
- [7] L. A. Coldren, S. W. Corzine, and M. L. Mašanović, *Diode Lasers and Photonic Integrated Circuits*. Wiley, Feb. 2012.
- [8] K. Iga, "Vertical-cavity surface-emitting laser: Its conception and evolution," *Japanese Journal of Applied Physics*, vol. 47, no. 1R, p. 1, Jan. 2008.
- [9] F. Koyama, S. Kinoshita, and K. Iga, "Room-temperature continuous wave lasing characteristics of a GaAs vertical cavity surface-emitting laser," *Applied Physics Letters*, vol. 55, no. 3, p. 221–222, Jul. 1989.
- [10] J. Jewell, K. Huang, K. Tai, Y. Lee, R. Fischer, S. McCall, and A. Cho, "Vertical cavity single quantum well laser," in *Conference on Lasers and Electro-Optics*. Optica Publishing Group, 1989, p. CPD14.
- [11] H. Uenohara, F. Koyama, and K. Iga, "Application of the multiquantum well (MQW) to a surface emitting laser," *Japanese Journal of Applied Physics*, vol. 28, no. 4R, p. 740, Apr. 1989.
- [12] Apple. (2017) Apple awards Finisar \$390 million from its advanced manufacturing fund. [Online]. Available: <https://www.apple.com/newsroom/2017/12/apple-awards-finisar-390-million-from-its-advanced-manufacturing-fund/>
- [13] R. Michalzik, *VCSELs: Fundamentals, Technology and Applications of Vertical-Cavity Surface-Emitting Lasers*. Berlin Heidelberg: Springer, 2013.
- [14] R. H. Johnson and D. M. Kuchta, "30 Gb/s directly modulated 850 nm datacom VCSELs," in *Conference on Lasers and Electro-Optics/Quantum Electronics and Laser Science Conference and Photonic Applications Systems Technologies*. Optica Publishing Group, 2008, p. CPDB2.

-
- [15] P. Westbergh, R. Safaisini, E. Haglund, J. S. Gustavsson, A. Larsson, M. Geen, R. Lawrence, and A. Joel, "High-speed oxide confined 850-nm VCSELs operating error-free at 40 Gb/s up to 85°C," *IEEE Photonics Technology Letters*, vol. 25, no. 8, pp. 768–771, 2013.
- [16] J. Ko, E. Hegblom, Y. Akulova, B. Thibeault, and L. Coldren, "Low-threshold 840-nm laterally oxidized vertical-cavity lasers using AlInGaAs-AlGaAs strained active layers," *IEEE Photonics Technology Letters*, vol. 9, no. 7, pp. 863–865, 1997.
- [17] H. Kuo, Y. Chang, F. Lai, T. Hsueh, L. Laih, and S. Wang, "High-speed modulation of 850 nm InGaAsP/InGaP strain-compensated VCSELs," *Electronics Letters*, vol. 39, no. 14, p. 1051–1053, Jul. 2003.
- [18] J. L. Jewell, Y. H. Lee, S. Walker, A. Scherer, J. P. Harbison, L. T. Florez, and S. L. McCall, "Low threshold electrically pumped vertical cavity surface emitting microlasers," in *Annual Meeting Optical Society of America*. Optica Publishing Group, 1989, p. TUP6. [Online]. Available: <https://opg.optica.org/abstract.cfm?URI=OAM-1989-TUP6>
- [19] M. Orenstein, A. C. von Lehmen, C. Chang-Hasnain, N. G. Stoffel, J. P. Harbison, L. T. Florez, E. Clausen, and J. E. Jewell, "Vertical-cavity surface-emitting InGaAs/GaAs lasers with planar lateral definition," *Applied Physics Letters*, vol. 56, no. 24, pp. 2384–2386, Jun. 1990.
- [20] K. Choquette, "Selectively-oxidized VCSELs after 3 decades," 2024, IEEE International Semiconductor Laser Conference.
- [21] L. W. Casperson, "Beam modes in complex lenslike media and resonators," *J. Opt. Soc. Am.*, vol. 66, no. 12, pp. 1373–1379, Dec 1976.
- [22] P. Westbergh, "High speed vertical cavity surface emitting lasers for short reach communication," PhD thesis, Chalmers University of Technology, Gothenburg, Sweden, April 2011.
- [23] R. Olshansky, P. Hill, V. Lanzisera, and W. Powazinik, "Frequency response of 1.3 μ m InGaAsP high speed semiconductor lasers," *IEEE Journal of Quantum Electronics*, vol. 23, no. 9, p. 1410–1418, Sep. 1987.

- [24] P. P. Baveja, B. Kögel, P. Westbergh, J. S. Gustavsson, Å. Haglund, D. N. Maywar, G. P. Agrawal, and A. Larsson, “Assessment of VCSEL thermal rollover mechanisms from measurements and empirical modeling,” *Opt. Express*, vol. 19, no. 16, pp. 15 490–15 505, Aug. 2011.
- [25] M. Daubenschütz and R. Michalzik, “Parameter extraction from temperature-dependent light-current-voltage data of vertical-cavity surface-emitting lasers,” in *Semiconductor Lasers and Laser Dynamics VII*, K. Panajotov, M. Sciamanna, A. Valle, and R. Michalzik, Eds., vol. 9892, International Society for Optics and Photonics. SPIE, 2016, p. 98920R.
- [26] Y. Varshni, “Temperature dependence of the energy gap in semiconductors,” *Physica*, vol. 34, no. 1, pp. 149–154, 1967.
- [27] S. Corzine, J. Scott, R. Geels, D. Young, B. Thibeault, M. Peters, and L. Coldren, “Reducing the effects of temperature on the threshold current of vertical-cavity surface-emitting lasers,” in *Summer Topical Meeting Digest on Broadband Analog and Digital Optoelectronics, Optical Multiple Access Networks, Integrated Optoelectronics, Smart Pixels*. IEEE, p. B51–B52.
- [28] J. Zhang, X. Zhang, H. Zhu, J. Zhang, Y. Ning, L. Qin, and L. Wang, “High-temperature operating 894.6nm-VCSELs with extremely low threshold for Cs-based chip scale atomic clocks,” *Opt. Express*, vol. 23, no. 11, pp. 14 763–14 773, Jun 2015.
- [29] S. L. Chuang, *Physics of Optoelectronic Devices*. New York: Wiley, 1995.
- [30] P. Derry, R. Fu, C. Hong, E. Chan, and L. Figueroa, “Analysis of the high temperature characteristics of InGaAs-AlGaAs strained quantum-well lasers,” *IEEE Journal of Quantum Electronics*, vol. 28, no. 12, pp. 2698–2705, 1992.
- [31] S. L. Chuang, “Efficient band-structure calculations of strained quantum wells,” *Phys. Rev. B*, vol. 43, pp. 9649–9661, Apr 1991.
- [32] N. C. Strategies, *SimuLase*, ver 3.0 ed., Nonlinear Control Strategies, 2021, available at <https://www.nlcstr.com/product/simulase/>.

-
- [33] J. Hader, N. Linder, and G. H. Döhler, “k·p theory of the Franz-Keldysh effect,” *Phys. Rev. B*, vol. 55, pp. 6960–6974, Mar. 1997.
- [34] M. Lindberg and S. W. Koch, “Effective Bloch equations for semiconductors,” *Phys. Rev. B*, vol. 38, pp. 3342–3350, Aug. 1988.
- [35] H. Haug and S. W. Koch, *Quantum Theory of the Optical and Electronic Properties of Semiconductors*. World Scientific, Jan. 2009.
- [36] I. Fritz, J. Klem, M. Hafich, A. Howard, and H. Hjalmarson, “Broadband light-emitting diode for 1.4 - 2.0 μm using variable-composition InGaAs quantum wells,” *IEEE Photonics Technology Letters*, vol. 7, no. 11, pp. 1270–1272, 1995.
- [37] M. Kajita, T. Kawakami, M. Nido, A. Kimura, T. Yoshikawa, K. Kurihara, Y. Sugimoto, and K. Kasahara, “Temperature characteristics of a vertical-cavity surface-emitting laser with a broad-gain bandwidth,” *IEEE Journal of Selected Topics in Quantum Electronics*, vol. 1, no. 2, pp. 654–660, 1995.
- [38] R. King, “VCSEL design for automotive datacom: Experimental results for 980 nm versus 850 nm,” TRUMPF Photonic Components GmbH, Tech. Rep., May 2021.
- [39] “IEEE standard for Ethernet amendment 7: Physical layer specifications and management parameters for multi-gigabit glass optical fiber automotive ethernet,” *IEEE Std 802.3cz-2023 (Amendment to IEEE Std 802.3-2022 as amended by IEEE Std 802.3dd-2022, IEEE Std 802.3cs-2022, IEEE Std 802.3db-2022, IEEE Std 802.3ck-2022, IEEE Std 802.3de-2022, and IEEE Std 802.3cx-2023)*, pp. 1–158, 2023.

REFERENCES
